Electronic Structure and Chemical Nature of Oxygen Dopant States in Carbon Nanotubes

Xuedan Ma,[†] Lyudmyla Adamska,[‡] Hisato Yamaguchi,[†] Sibel Ebru Yalcin,[†] Sergei Tretiak,[†,‡] Stephen K. Doorn,[*,†] and Han Htoon[*,†]

[†]Center for Integrated Nanotechnologies, Materials Physics and Applications Division, [‡]Theory Division, Los Alamos National Laboratory, Los Alamos, New Mexico 87545, United States

ABSTRACT We performed low temperature photoluminescence (PL) studies on individual oxygen-doped single-walled carbon nanotubes (SWCNTs) and correlated our observations to electronic structure simulations. Our experiment reveals multiple sharp asymmetric emission peaks at energies 50−300 meV red-shifted from that of the E_{11} bright exciton peak. Our simulation suggests an association of these peaks with deep trap states tied to different specific chemical adducts. In addition, oxygen doping is also observed to split the E_{11} exciton into two or more states with an energy splitting <40 meV. We attribute these states to dark states that are brightened through defect-induced symmetry breaking. While the wave functions of these brightened states are delocalized, those of the deep-trap states are strongly localized and pinned to the dopants. These findings are consistent with our experimental observation of asymmetric broadening of the deep trap emission peaks, which can result from interaction between pinned excitons and one-dimensional phonons. Exciton pinning also increases the sensitivity of the deep traps to the local dielectric environment, leading to a large inhomogeneous broadening. Observations of multiple spectral features on single nanotubes indicate the possibility of different chemical adducts coexisting on a given nanotube.

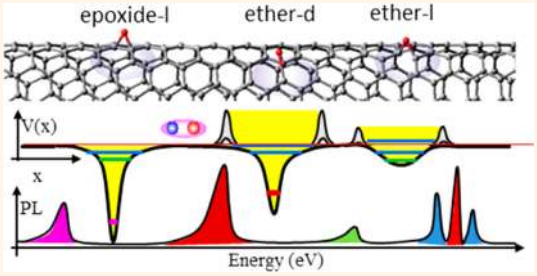

KEYWORDS: carbon nanotubes · electronic structure · oxygen doping · photoluminescence · exciton localization

Unique electronic and optical properties of one-dimensional (1D), semiconducting single-walled carbon nanotubes (SWCNTs) have inspired a wide range of optoelectronic,[1] sensing,[2] imaging[3] and quantum communication[4−6] applications. A major barrier to practical realization of these applications is the low SWCNT fluorescence quantum yield (QY, typically ~1% for ensemble measurements in surfactant suspensions).[7−13] Although QY values approaching 10% are reported for the brightest individual nanotubes in such samples,[8] in solution samples engineered to protect the nanotube from environmental influences,[14,15] and for air-suspended nanotubes,[16] these results underscore the importance of the nanotube surface environment and sample quality as major factors in determining QY. Furthermore, the existence of optically forbidden "dark" states that lie below the lowest optically allowed bright state[17−22] and nonradiative recombination of freely diffusing 1D excitons at defect sites[23−27] are attributed as key factors limiting the QY of SWCNTs. This limitation could, in principle, be removed *via* the introduction of a highly emissive deep trap state below the dark exciton.[28] Recent studies revealed that such a state can be created through incorporation of low-level oxygen[29,30] or diazonium[31] covalently bound dopants on the side walls of SWCNTs. Previously, a number of other routes have also been demonstrated for introducing similar states, with examples including photoinduced behaviors,[32−34] symmetry breaking following chemisorption,[35,36] and chemical or electrochemical trion generation.[37−39] Oxygen and diazonium doping approaches,[29,31] however, stand out from these prior studies because covalent modification introduces chemically stable sites with remarkably bright deep trap emission.

These discoveries have triggered intense interest in such covalently doped SWCNTs. However, a fundamental understanding of the electronic structures of these covalently

* Address correspondence to skdoorn@lanl.gov, htoon@lanl.gov.

Received for review August 14, 2014 and accepted September 29, 2014.

Published online September 29, 2014
10.1021/nn504553y

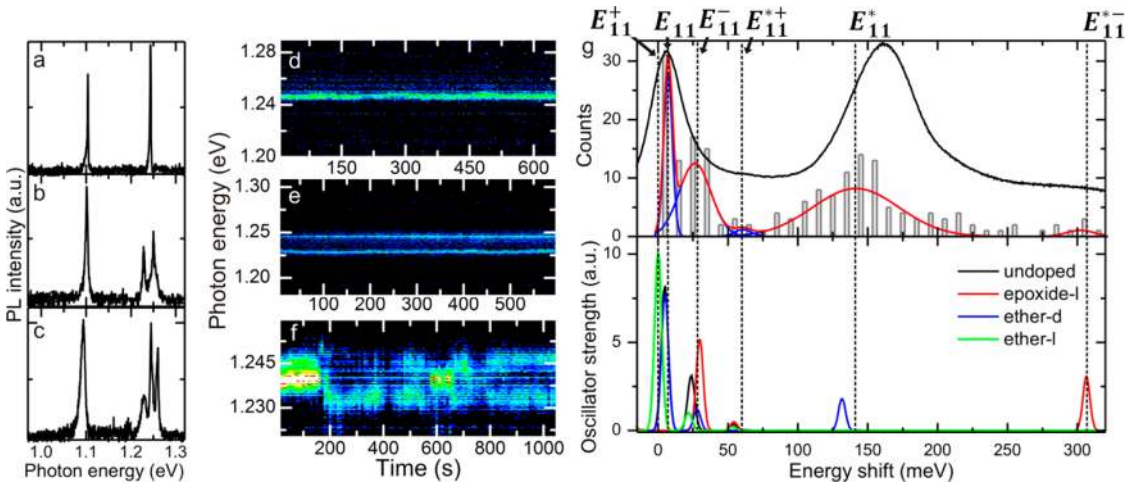

Figure 1. (a−c) Representative spectra of three oxygen-doped SWCNTs showing the deep trap (E_{11}^{*}) state at ~1.1 eV, and with one (a), two (b), and three (c) peak features at ~1.25 eV spectral range. (d−f) Temporal evolution of spectral features in the vicinity of E_{11} transitions of three individual SWCNTs. (g) Upper panel: a histogram of experimentally observed spectral features in oxygen-doped SWCNTs (bars). The peak positions are plotted relative to the highest energy peak (vertical dashed line marked as E_{11}^{+}). Blue and red solid lines are Gaussian fits to each distribution peak and the sum of all the fits, respectively. Room temperature ensemble PL spectrum is plotted in black for comparison. Lower panel: theoretically calculated absorption spectra of different electronic states in undoped SWCNTs (black curve) and oxygen-doped SWCNTs with different functional groups. The energy of the lowest bright state of SWCNT functionalized with ether-l is set to zero (E_{11}^{+}). A 5 meV Gaussian smearing is applied to generate all absorption spectra.

introduced trap-states, exact chemical nature of dopants and the mechanisms responsible for the enhancement of QY are still lacking. Some experimental[29−31] and theoretical[40,41] studies attributed these deep traps to spatially localized exciton states resulting from splitting of degenerate energy levels by the dopants.[30] However, calculations of Mu *et al.*[42] argued that the observed red-shifted peak, which is commonly referred to as E_{11}^{*}, is simply a strong Stokes shift and the excitons remain delocalized. Furthermore, a significantly broader ensemble PL spectrum of trap states compared to that of the intrinsic peak[29,30] raises the question of whether the trap states have intrinsically broad optical transitions or if broadening results from environmental inhomogeneity.

To address these outstanding issues, we performed a low temperature (low T) photoluminescence (PL) spectroscopy study on individual oxygen-doped SWCNTs. In addition to the well-known deep-trap state (E_{11}^{*}) located 135 meV (ΔE) below the intrinsic 1D bright exciton (E_{11}),[29,30] we discovered that oxygen doping splits E_{11} into two or more states with an energy splitting <40 meV and creates two more deep-trap states (E_{11}^{*+}, E_{11}^{*-}) at ΔEs of 55 and 300 meV. All the deep trap states are characterized by sharp asymmetric spectral lines with widths of ~6.38 ± 3.46 meV. Their positions, however, exhibit a broad inhomogeneous distribution that closely resembles ensemble PL spectra.[29,30] Through time dependent density functional simulations, we identify the oxygen functional groups responsible for the observed spectral features and show that multiple distinct functional groups may coexist on a single SWCNT. We also explain the asymmetric line shape and strong inhomogeneous distribution of deep trap states as a consequence of exciton pinning by the dopants.

RESULTS AND DISCUSSION

In this study, we excite individual oxygen doped (6,5) SWCNTs (generated *via* ozonolysis[29]) at the E_{11} phonon sideband. For reference, we also characterized undoped SWCNTs prepared in the same manner except for ozonation. Low T PL images of both undoped and ozonated tubes show diffraction limited circular spots (Supporting Information Figure S1c,d) indicating that PL originates from a region of less than 1 μm. Emission peaks of all 24 investigated undoped tubes lie in the range of 1.2−1.28 meV and 21 of them (*i.e.*, 88%) displayed a single sharp, symmetric PL peak with line widths of 4.4 ± 1.4 meV (Supporting Information Figure S2).[4,6,43] These PL peaks are also nearly free of both intensity and spectral fluctuations (Supporting Information Figure S2b). These reference data point to the fact that our undoped control sample exhibits only the optical behavior of (6,5) tubes and is therefore free of any unintentional dopants, defects and charges that could introduce new optical transitions. We can therefore safely attribute any new optical transitions displayed by the ozonated samples to the effect of oxygen doping.

In the case of oxygen-doped tubes, the deep trap emission peak reported in prior studies[29,30] was observed for all the doped tubes in the 1.06−1.15 eV PL spectral range (Figure 1a−c). However, surprisingly, we also observed multiple spectral features that have not been reported before (Figure 1b,c and Figure 2a−d).

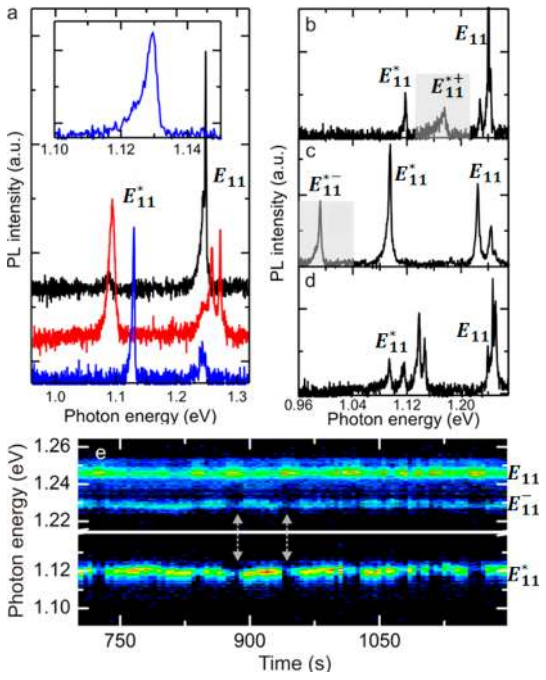

Figure 2. (a) PL spectra from three oxygen-doped SWCNTs with different intensity ratios between the E_{11} (1.25 eV) and E_{11}^* (1.10 eV) peaks. Inset: the enlarged view of the E_{11}^* peak of the bottom PL spectrum (blue curve) clearly shows asymmetric broadening of the peak. (b−d) Representative PL spectra of three oxygen-doped SWCNTs showing multiple deep trap emission peaks. (e) Temporal evolution of PL spectra of an individual oxygen-doped SWCNT showing anticorrelated PL intensity fluctuation between E_{11} and trap related emissions (E_{11}^- and E_{11}^*). Gray arrows mark the clearest examples of positive and negative correlations.

We first describe additional peaks appearing near the original E_{11} peak. We observed that only 27% (20 out of 74) of ozonated SWCNTs show a single sharp E_{11} peak at ~1.25 eV (Figure 1a). A two- or three-peak spectral feature was observed for the remaining 73% of the tubes (Figure 1b,c). Similar features were also observed in PL spectra of ozonated SWCNTs excited at 561 nm (Supporting Information S2 and Figure S4), confirming that these peaks have PL origin and are not the result of a Raman process. While some doped SWCNTs exhibit stable PL in terms of both intensity and peak position (Figure 1d and 1e), others show rapid fluctuation in both (Figure 1f). In cases like this, a single emission peak appears to split into two peaks. The three-peak spectral features of some ozonated tubes observed in Figure 1c could in fact result from time integration of such fluctuating spectra. Fitting all the E_{11} PL peaks with Lorentzian functions gives an average peak position of 1.24 ± 0.0194 eV and line width of 5.30 ± 3.301 meV (Supporting Information Figure S3), comparable to those of the undoped tubes. Although absolute positions of the split E_{11} peaks are distributed over the range of 1.19−1.31 eV for different individual doped tubes, peak to peak energy separations measured relative to the highest energy peak exhibit a bimodal distribution, with energies shifted from this reference peak by 7.1 and 26 meV with the distribution widths of 7.2 and 26.7 meV, respectively. The reference peak at 0 eV and the two distributions are marked as E_{11}^+, E_{11}, and E_{11}^-, respectively, in the histogram of Figure 1g. These data provide clear evidence that oxygen doping not only creates a deep trap E_{11}^*state, but may also split the E_{11} transition into 2−3 states.

Next we discuss the spectral features of doping-introduced deep-trap states. While 47% out of 74 doped tubes show a single deep trap emission peak (Figure 2a), 53% of the tubes show multiple peaks as displayed in Figure 2b-2d. Positions and distribution of these peaks vary widely between tubes. The histogram of all deep trap emission peaks shows three distinct distributions centered at 55, 135, and 300 meV, labeled as E_{11}^{*+}, E_{11}^*, and E_{11}^{*-}, respectively, in Figure 1g, upper panel. E_{11}^*, the most dominant feature, aligns well with that of the ensemble PL spectrum and also exhibits a comparable line width of ~60 meV in the histogram distribution. E_{11}^{*+} and E_{11}^{*-} peaks appear only in 24% of the tubes. These findings together with the fact that low T PL spectra of undoped reference tubes show no PL peak in this spectral regime (Supporting Information Figure S2c) suggest the existence of one dominant chemical functional group responsible for the E_{11}^* peak and other less abundant functional group-(s) responsible for E_{11}^{*+} and E_{11}^{*-} peaks. In the following, we will identify these functional groups by comparing experimental spectra with the results of quantum-chemical calculations.

Despite wide variation in emission energy, individual deep trap emission peaks exhibit a very narrow spectral line width of 6.38 ± 3.46 meV, only slightly broader than that for E_{11} (5.30 ± 3.301 meV). More interestingly, the peaks observed in 83% of the doped tubes appear highly asymmetric with a long tail on the low energy side (Figure 2a, inset). These findings lead us to conclude that individual sharp peaks originate from a single trap site and their emission energies are inhomogeneously distributed due to variation of the local dielectric environment, as is known to occur in the case of E_{11} emission peaks.[4,6,43] The larger distribution range of the E_{11}^* peak (~60 meV) compared to that of E_{11} (~30 meV, see Supporting Information Figures S5a and S3a) further suggests that environmental fluctuations such as variation in surfactant coverage along the length of the nanotube[24] have a stronger influence on the deep trap E_{11}^* state than on the E_{11} state.

Similar to the E_{11} peak, E_{11}^* peaks also display PL intensity and spectral fluctuations (Figure 2e and Supporting Information Figures S6 and S7). While fluctuations observed in some SWCNTs are completely random, in some cases, we observed very interesting correlations among E_{11}, E_{11}^-, and E_{11}^* peaks. Figure 2e shows that while intensity fluctuations of E_{11}^-, and E_{11}^* correlate with one another, both fluctuate in negative correlation with the E_{11} peak (see Supporting Information S4 for

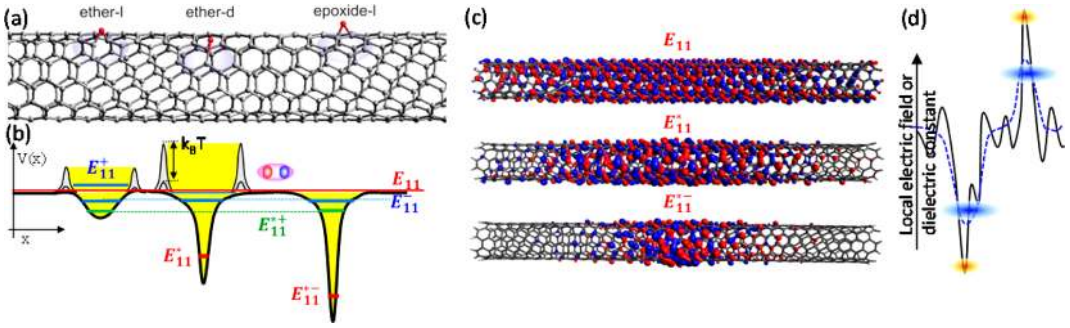

Figure 3. (a) Structure of ether-l (left), ether-d (center), and epoxide-l (right) adducts on a segment of (6,5) SWCNT. (b) Schematic of potential profile along the length of the tube showing potential traps created by ether-l (left), ether-d (center), and epoxide-l (right) adducts. Deep trap states and states that result from the brightening of dark states are marked with brown and blue lines, respectively. Bright exciton state of undoped tube is represented by the red line. Fluctuation of small potential barriers in the vicinity of the trap site leads to fluctuation of exciton trapping efficiency and negatively correlated PL intensity fluctuations between E_{11} and dopant related emissions (*i.e.*, E_{11}^* and E_{11}^-). (c) The spatial distributions of transition densities for E_{11} (top), E_{11}^* (middle), and E_{11}^{*-} (bottom). The electrons and holes are represented in red and blue, respectively. While E_{11} excitons in undoped SWCNTs are delocalized, E_{11}^* exciton of ether-d and E_{11}^{*-} exciton of epoxy-l functionalities are localized strongly. (d) Schematic illustration of environmental effects (*e.g.*, fluctuations in local electric field or dielectric constant). While excitons pinned to 3−4 nm region of the traps (orange ellipses) experience the full extent of the fluctuation (black solid lines), delocalized E_{11} excitons "see" smoother fluctuations (blue dashed line) due to spatial averaging over the extent of its wave function represented by the blue ellipses.

calculation of correlation coefficients and more examples of spectroscopic data). Because migration as well as attachment/detachment of dopants are unlikely at cryogenic temperatures, we attribute these fluctuations to variations in internal conversion processes, where the E_{11}^* and E_{11}^- states together compete against the E_{11} state for exciton population.

To further elucidate these findings, we calculated the electronic structure of oxygen-doped (6,5) SWCNTs using semiempirical and density functional theory (DFT) methods, which have successfully modeled multiple electronic phenomena in undoped[44] as well as doped tubes.[40,41] (see Supporting Information S5). Our calculations identify ether-d (d: C−O−C bonds perpendicular to the tube axis) as the most stable oxygen adduct with the highest binding energy of −5.28 eV and epoxide-l and ether-l (l: C−O−C bonds parallel to the tube axis) as less stable adducts with binding energies of −3.75 and −2.81 eV, respectively (Figure 3a, Supporting Information S5). The time-dependent DFT (TDDFT) calculations yield multiple electronic transitions for each adduct that align with the peaks of the histogram (Figure 1g, lower panel). Specifically, when the first of the ether-l transitions is set to align with the 0 meV reference of the histogram (*i.e.*, E_{11}^+, the highest energy peak of the PL spectrum), we can match the E_{11} peak with the first transitions of ether-d and undoped tubes overlapping at 7 meV, and E_{11}^- with a group of peaks composed of ether-l at 22 meV, ether-d at 28 meV, epoxide-l at 30 meV, and undoped tubes at 24 meV. Ether-l, epoxide-l, and undoped tubes have transitions at 55 meV that align with the E_{11}^{*+} peak. E_{11}^* and E_{11}^{*-} peaks align very well with the lowest energy transitions of ether-d and epoxide-l at 131 and 306 meV, respectively. While these two lowest energy transitions are the deep trap states introduced by the dopants, the remaining higher energy transitions (those aligned with E_{11}^+, E_{11}, E_{11}^-, and E_{11}^{*+}) result from partial transfer of oscillator strength from the E_{11} bright state to close-lying dark states (brightening) due to symmetry breaking. In the case of undoped tubes, symmetry breaking happens at the ends of the 8 nm long tube which causes artificial brightening of the state lying at 55 meV. The intensity of this peak is greatly reduced in longer tubes (see Computational Methods for more details). Therefore, only a single E_{11} peak is expected to appear in our PL spectra of undoped tubes, which are 0.6−6 μm long. In the case of doped tubes, dopant induced symmetry breaking leads to the emergence of the E_{11}^+, E_{11}, E_{11}^-, and E_{11}^{*+} peaks. The electronic structures of ether-l, ether-d, and epoxide-d revealed in these calculations are schematically illustrated in Figure 3b. The high degree of alignment we find between the TDDFT results and the experimental features then provides a strong basis for assignment of spectral features to specific adducts, as noted in Table 1.

TABLE 1. A Table of Dopant Induced Optical Transitions, Their Energy Separation (ΔE) from the Reference Peak, and Chemical Functional Groups Responsible for the Transitions[a]

transitions	ΔE (meV)	functional group
E_{11}^+	0	ether-l
E_{11}	7	undoped, ether-d
E_{11}^-	∼26	ether-l, ether-d, epoxide-l
E_{11}^{*+}	55	ether-l, epoxide-l
E_{11}^*	135	ether-d
E_{11}^{*-}	310	epoxide-l

[a] The ΔE values were obtained from the simulation and Gaussian fit to the histogram of Figure 1.

In particular, these results are consistent with an assignment of the E_{11}^{-} and E_{11}^{*} peaks that appear in almost all of the PL spectra of doped tubes to the most stable adduct, ether-d. This assignment also explains the correlated PL intensity fluctuation of the E_{11}^{-} and E_{11}^{*} peaks reported in Figure 2e and Supporting Information Figures S6 and S7. The negative correlation between E_{11} and E_{11}^{*}, on the other hand, suggests that the PL of E_{11} originates from the undoped portion of the tube. We further speculate that existence of a potential barrier higher than k_BT, as illustrated in Figure 3, may prevent the E_{11} exciton from trapping and encourage recombination in the undoped region. Thermal fluctuation of such a barrier could cause the observed increase/decrease in PL intensity of the E_{11} peak with a correlated decrease/increase in PL of E_{11}^{*} and E_{11}^{-} peaks.

With the TDDFT results suggesting that the E_{11}^{*+}, E_{11}^{*-}, and E_{11}^{*} peaks originate from different chemical species, the simultaneous appearance of E_{11}^{*+} and E_{11}^{*-} peaks with E_{11}^{*} in some PL spectra (*e.g.*, Figure 2b,c) suggests that ether-l and epoxide-l adducts may coexist with the ether-d adducts on the same tube. Lower stability of these adducts explains why these peaks appear only in 24% of the doped tubes. Some of the E_{11}^{+} peaks that fluctuate in correlation with E_{11}^{-} peaks (*e.g.*, Figure 1f) may also be attributed to coexistence of ether-l and ether-d. Conversely, the spectrum of Figure 2d also demonstrates that multiple ether-d sites may be present on a single tube, but display different transition energies due to each site experiencing a different dielectric environment.

Next, using TDDFT modeling, we calculated spatial distributions of transition densities that directly evaluate real-space exciton distributions of the relevant electronic states (*i.e.*, spatial delocalization of the excitonic center of mass on the tube). Our transition density plots show that while excitons of the higher energy states (*i.e.*, E_{11}^{+} and E_{11}^{-}) are delocalized over the 8 nm length of our model tube due to hybridization with the E_{11} excitonic band of the undoped tube, those of the lowest energy trap states (*i.e.*, E_{11}^{*} and E_{11}^{*-}) are spatially localized and pinned to a 3−4 nm region around the respective dopant sites (Figure 3c and Supporting Information Figure S9). The dopant-induced localization provides a basis for the origin of the asymmetric line shape of the deep trap emission. Such asymmetric broadening of E_{11} spectral lines is occasionally observed in low T PL spectra[43,45,46] and has been explained as arising from interaction between 0D exciton states and 1D acoustic phonons.[45,46] With exciton localization being the key requirement to facilitate this coupling, this suggests that interaction between our dopant-pinned 0D excitons and 1D acoustic phonons of SWCNTs is responsible for the asymmetric broadening of the deep-trap spectral lines. The existence of dopants ensures exciton pinning and asymmetric broadening in all of the doped tubes.

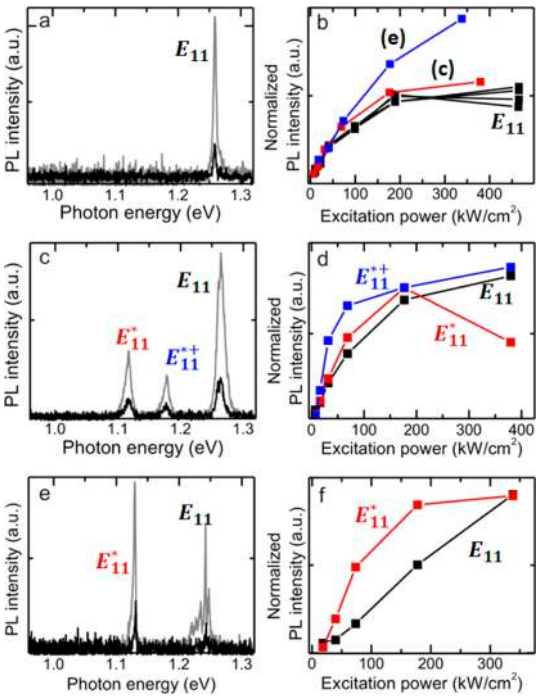

Figure 4. (a, c, and e) Low T PL spectra of an undoped (a) and two ozonated (c and e) tubes at low (black) and high (gray) pump powers. (b) Normalized spectrally integrated total PL intensity of 4 undoped SWCNT showing E_{11} saturation at ~200 kW/cm^2 (black lines and data points) and that of ozonated tubes shown in (c) (red) and (e) (blue) showing weaker saturation. (d and f) PL saturation behavior of E_{11} (black), E_{11}^{*+} (blue), and E_{11}^{*} (red) peaks.

To further confirm this point, we estimated a reorganization energy (RE) that provides a measure of the coupling between the trapped exciton and all the phonon modes of the SWCNT from the difference between total energies in optimized geometries of the ground and excited states. The calculations reveal nearly a factor of 2 increase of RE from 11 meV in undoped tubes to 18 meV for the ether-d adduct, suggesting that acoustic phonon coupling may increase along with coupling to other phonon modes.

We can also attribute exciton pinning to the enhancement of environmental effects that give rise to the large inhomogeneous broadening of deep trap emission. Fluctuations of local electric field or local dielectric constant are known to cause a distribution of E_{11} emission at low temperature through a quantum confined Stark effect. Such fluctuations may occur from local variation in the nanotube surface environment, including changes in surfactant structure and composition. It is conceivable that these fluctuations are happening at a length scale smaller than the wave function of the E_{11} exciton as schematically demonstrated by the solid line in Figure 3d. In that case, the E_{11} exciton will only experience the smoother fluctuations (blue dashed line) resulting from spatial averaging of the fluctuations over the extent of its wave function (represented by the blue ellipse). On the

other hand, since excitons of deep trap states (orange ellipses) are pinned to a region smaller than the environmental fluctuations, they experience the full extent of the fluctuations and hence exhibit a much broader inhomogeneous distribution. In addition to the Stark effect, variation of local surfactants and surface charges could also lead to small variations in the geometry of the dopant sites and shift their emission energy.

One additional, potentially beneficial consequence of the dopant-induced exciton pinning appears in the pump power dependent evolution of the PL spectra. PL of undoped tubes shows saturation (Figure 4a,b) at pump powers of ~200 kW/cm^2 due to exciton−exciton annihilation (EEA).[47,48] Somewhat similar saturation behavior can be observed for the E_{11}^{*-} and E_{11}^{*} deep trap states (Figure 4c−f) due to saturation of deep traps. However, saturation behavior of the E_{11} peak becomes weaker with an increase of deep trap state emission. Specifically, for the SWCNT of Figure 4c in which E_{11} emission is stronger compared to emission of both $E_{11}^{*\mp}$ and E_{11}^{*} peaks, E_{11} exhibits a saturation behavior slightly weaker than that observed in undoped tubes (Figure 4b). However, for the SWCNT of Figure 4e, in which the E_{11}^{*} peak is stronger than the E_{11} peak, the E_{11} peak now shows a nearly linear increase of PL with pump power (Figure 4f, see Supporting Information Figure S10 for more examples). As a result, PL saturation behavior of total spectrally integrated PL of the ozonated tubes becomes weaker with the strengthening of the E_{11}^{*} peaks (red and blue traces of Figure 4b). These findings suggest that the efficient trapping of excitons by the oxygen dopant leads not only to strong trap emission (*i.e.*, E_{11}^{*} and E_{11}^{*+}), but also to reduction of the E_{11} exciton population, which effectively suppresses the EEA process. We can therefore conclude that doping provides an interesting route to suppress EEA processes and allows emission of excitons that would otherwise have recombined nonradiatively.

CONCLUSIONS

These findings and analyses bring a new level of understanding to the electronic structure and chemical nature of oxygen dopant states. Specifically, our study provides conclusive evidence that oxygen dopants indeed create traps deep enough for localizing excitons at room temperature. This localization prevents nonradiative collisional recombination of excitons. Emission of photons from such localized states could particularly be useful for room temperature single photon generation. Through TDDFT calculations, we identify three distinct chemical adducts (ether-d, ether-l, and epoxide-l) capable of creating these deep trap states and which can explain the observation of multiple deep trap emission features in our single tube PL spectra as a consequence of the coexistence of multiple adducts. Additionally, oxygen doping is also revealed to create several transitions that may arise from defect-induced symmetry breaking in the vicinity of E_{11} states. Overall, our work lays the foundation to utilize doping as a generalized route for wave function engineering and direct control of carrier dynamics in SWCNTs toward enhanced light emission properties for photonic applications.

MATERIALS AND METHODS

Sample Preparation. Oxygen-doped SWCNTs used in this study were prepared following the method in ref 29 with some modifications. Briefly, 1 wt % sodium deoxycholate (DOC) wrapped HiPco SWCNT supernatants were chirality-sorted *via* density gradient ultracentrifugation[49,50] and fractions enriched in (6,5) SWCNTs were dialyzed into 1 wt % sodium dodecylbenzenesulfonate (SDBS). This enriched (6,5) sample in 1 wt % SDBS served as our final source material for preparing both the oxygen-doped SWCNTs and the undoped control sample. For oxygen doping, the (6,5) suspension was diluted with deionized (DI) water to decrease the SDBS concentration to 0.2 wt %. Ozone saturated water was then added to SWCNT suspensions (typically, 90 μL of ozonized water to 300 μL of SWCNT suspension), and the mixture was irradiated with a fluorescent lamp overnight (17 h). The SDBS concentration was increased back to 1 wt % after the ozonation treatments prior to the measurements. The same experimental procedure (including the dilution step, but without the addition of ozonated water) was applied to make the undoped control samples. To prepare samples for individual SWCNT PL measurements, a 5−10 μL drop of nanotube suspension was deposited on a precleaned, plasma-treated quartz substrate with density less than one nanotube per 10 × 10 μm^2 area and mounted in a continuous-flow, liquid-He cryostat.

Photoluminescence Imaging and Spectroscopy Measurements. All spectroscopy experiments were performed in the temperature range between 4.2 and 6.6 K. Single tube PL measurements were performed on a home-built confocal laser microscope. A continuous-wave (CW) Ti:sapphire laser operating at 820 nm and a 561 nm CW diode laser were used to excite (6,5) SWCNTs at their E_{11} phonon sideband and E_{22} resonance, respectively. Most of the experiments were conducted with the Ti:sapphire laser unless otherwise specified. An infrared objective with NA = 0.55 and 50× magnification was used to focus the laser beam and collect PL. PL signal from SWCNTs was spatially and spectrally imaged by a 2D InGaAs camera equipped on a 300 mm spectrograph and spectrally resolved by a linear InGaAs array equipped on a 150 mm spectrograph with integration time typically between 1 and 30 s.

Computational Methods. All computations were performed on finite length (6,5) SWCNTs with the edges terminated by hydrogens as detailed in ref 44. Such quantum-chemical simulations of finite tube length are well suited to study inhomogeneous structures (from amorphous materials to perfect periodic systems), various disorders, local defects, chemical functionalizations, intertube interactions, *etc.*[40,41,44,51] The length of all calculated tubes was set to 8 nm to be larger than the typical exciton size (electron hole separation) and to allow numerical feasibility of various quantum-chemical methods. Three different atomic structures including epoxide (oxygen bridging carbon sites), ether (oxygen bridging two neighboring carbon atoms and the bond between the latter two is broken), and chemisorbed ozone (ozone binds on top of two neighboring carbon atoms), as well as different relative orientations of the structures (l, along tube axis; d, perpendicular to tube axis), were considered (see Supporting Information Figure S8).

Each dopant was placed in the middle of the tube. Semiempirical Austin Model 1 (AM1) Hamiltonian as implemented in the MOPAC program package[52] was used to optimize the ground state geometries of all structures. Binding energies and formation energies of the different functional groups/molecules (Supporting Information Table S1) were evaluated with AM1 method as well. Binding energies were calculated with respect to undoped tubes and O1 (for epoxide and ether)/O3 (for ozone) molecules, while formation energies were calculated with respect to undoped tubes and O2 (epoxide and ether)/O3 (ozone) molecules as reference systems. Compared to epoxide-l and ether-l, ether-d has the largest binding energy and therefore is the most stable structure, in agreement with ref 29.

Electronic transition energies (Supporting Information Table S1), their respective oscillator strengths and transition densities (Supporting Information Figure S9) of excitons in (6,5) SWCNTs with different functional groups were further modeled using TDDFT approach based on STO-3G basis set and B3LYP functional as implemented in Gaussian 09 program[53] package. The use of minimal basis set was motivated by the large system size. Due to high computational cost, the structures optimized by AM1 Hamiltonian method were not reoptimized with DFT and/or TDDFT. Our computation method has been extensively validated in the previous studies.[40,41,44] For example, a band gap of 1.76 eV obtained for undoped (6,5) SWCNTs agrees well with reported experimental results.[54] Absorption spectra were obtained by applying a 5 meV Gaussian smearing to the calculated oscillator strengths.

We performed the test calculations on longer undoped tubes (10 and 12 nm) and observed a significant reduction of the oscillator strength in the level located ~55 meV below E_{11}, which signifies the artificial brightening of this state in undoped tubes due to symmetry breaking at the ends of the 8 nm tube. The results for ether-d and epoxide-l doped 12 nm tubes are similar to those described in this work (8 nm) except that the distance between the undoped peak and E^*_{11}, $E^*_{11^-}$ levels slightly decreased. Due to the high computational complexity of the 12 nm calculations, we analyzed only optical spectra and did not address the orbital projection of transition density for localized excitons.

Conflict of Interest: The authors declare no competing financial interest.

Supporting Information Available: PL characteristics of undoped and oxygen-doped SWCNTs, PL spectra of oxygen-doped SWCNTs excited by a 561 nm laser, position and line width of the PL peaks at ~1.10 eV in oxygen-doped SWCNTs, PL fluctuations of deep trap states, computation of electronic properties of undoped and oxygen-doped (6,5) SWCNTs, exciton distribution in undoped and oxygen-doped SWCNTs, and additional examples of PL saturation behavior. This material is available free of charge *via* the Internet at http://pubs.acs.org.

Acknowledgment. This work was conducted, in part, at the Center for Integrated Nanotechnologies, a U.S. Department of Energy, Office of Basic Energy Sciences user facility and supported in part by Los Alamos National Laboratory (LANL) Directed Research and Development Funds. We thank Nicholas Parra-Vasquez of LANL for insightful discussion on ozonation chemistry of SWCNTs and Juan Duque of LANL for providing (6,5) enriched SWCNT samples. H.Y. acknowledges the LANL Director's postdoctoral fellowship for financial support.

REFERENCES AND NOTES

1. Avouris, P.; Freitag, M.; Perebeinos, V. Carbon-Nanotube Photonics and Optoelectronics. *Nat. Photonics* **2008**, *2*, 341–350.
2. Barone, P. W.; Baik, S.; Heller, D. A.; Strano, M. S. Near-Infrared Optical Sensors Based on Single-Walled Carbon Nanotubes. *Nat. Mater.* **2005**, *4*, 86–92.
3. Welsher, K.; Liu, Z.; Sherlock, S. P.; Robinson, J. T.; Chen, Z.; Daranciang, D.; Dai, H. J. A Route to Brightly Fluorescent Carbon Nanotubes for near-Infrared Imaging in Mice. *Nat. Nanotechnol.* **2009**, *4*, 773–780.
4. Hoegele, A.; Galland, C.; Winger, M.; Imamoglu, A. Photon Antibunching in the Photoluminescence Spectra of a Single Carbon Nanotube. *Phys. Rev. Lett.* **2008**, *100*, 217401.
5. Hofmann, M. S.; Glueckert, J. T.; Noe, J.; Bourjau, C.; Dehmel, R.; Hoegele, A. Bright, Long-Lived and Coherent Excitons in Carbon Nanotube Quantum Dots. *Nat. Nanotechnol.* **2013**, *8* (7), 502–505.
6. Walden-Newman, W.; Sarpkaya, I.; Strauf, S. Quantum Light Signatures and Nanosecond Spectral Diffusion from Cavity-Embedded Carbon Nanotubes. *Nano Lett.* **2012**, *12*, 1934–1941.
7. Crochet, J.; Clemens, M.; Hertel, T. Quantum Yield Heterogeneities of Aqueous Single-Wall Carbon Nanotube Suspensions. *J. Am. Chem. Soc.* **2007**, *129*, 8058–8059.
8. Tsyboulski, D. A.; Rocha, J.-D. R.; Bachilo, S. M.; Cognet, L.; Weisman, R. B. Structure-Dependent Fluorescence Efficiencies in Single-Walled Carbon Nanotubes. *Nano Lett.* **2007**, *7*, 3080–3085.
9. Carlson, L. J.; Maccagnano, S. E.; Zheng, M.; Silcox, J.; Krauss, T. D. Fluorescence Efficiency of Individual Carbon Nanotubes. *Nano Lett.* **2007**, *7*, 3698–3703.
10. Miyauchi, Y.; Hirori, H.; Matsuda, K.; Kanemitsu, Y. Radiative Lifetimes and Coherence Lengths of One-Dimensional Excitons in Single-Walled Carbon Nanotubes. *Phys. Rev. B* **2009**, *80*, 081410(R).
11. Hertel, T.; Himmelein, S.; Ackermann, T.; Stich, D.; Crochet, J. Diffusion Limited Photoluminescence Quantum Yields in 1-D Semiconductors: Single-Wall Carbon Nanotubes. *ACS Nano* **2010**, *4*, 7161–7168.
12. Mouri, S.; Miyauchi, Y.; Matsuda, K. Dispersion-Process Effects on the Photoluminescence Quantum Yields of Single-Walled Carbon Nanotubes Dispersed Using Aromatic Polymers. *J. Phys. Chem. C* **2012**, *116*, 10282–10286.
13. Berciaud, S.; Cognet, L.; Lounis, B. Luminescence Decay and the Absorption Cross Section of Individual Single-Walled Carbon Nanotubes. *Phys. Rev. Lett.* **2008**, *101*, 077402.
14. Ju, S.-Y.; Kopcha, W. P.; Papadimitrakopoulos, F. Brightly Fluorescent Single-Walled Carbon Nanotubes *via* an Oxygen-Excluding Surfactant Organization. *Science* **2009**, *323*, 1319–1323.
15. Lee, A. J.; Wang, X.; Carlson, L. J.; Smyder, J. A.; Loesch, B.; Tu, X.; Zheng, M.; Krauss, T. D. Bright Fluorescence from Individual Single-Walled Carbon Nanotubes. *Nano Lett.* **2011**, *11*, 1636–1640.
16. Lefebvre, J.; Austing, D. G.; Bond, J.; Finnie, P. Photoluminescence Imaging of Suspended Single-Walled Carbon Nanotubes. *Nano Lett.* **2006**, *6*, 1603.
17. Alfonsi, J.; Lanzani, G.; Meneghetti, M. Exact Diagonalization of Hubbard Models for the Optical Properties of Single-Wall Carbon Nanotubes. *New J. Phys.* **2010**, *12*, 083009.
18. Mortimer, I. B.; Nicholas, R. J. Role of Bright and Dark Excitons in the Temperature-Dependent Photoluminescence of Carbon Nanotubes. *Phys. Rev. Lett.* **2007**, *98*, 027404.
19. Perebeinos, V.; Tersoff, J.; Avouris, P. Radiative Lifetime of Excitons in Carbon Nanotubes. *Nano Lett.* **2005**, *5*, 2495–2499.
20. Shaver, J.; Kono, J.; Portugall, O.; Krstic, V.; Rikken, G. L. J. A.; Miyauchi, Y.; Maruyama, S.; Perebeinos, V. Magnetic Brightening of Carbon Nanotube Photoluminescence through Symmetry Breaking. *Nano Lett.* **2007**, *7*, 1851–1855.
21. Spataru, S. D.; Ismail-Beigi, S.; Capaz, R. B.; Louie, S. G. Theory and *ab Initio* Calculation of Radiative Lifetime of Excitons in Semiconducting Carbon Nanotubes. *Phys. Rev. Lett.* **2005**, *95*, 247402.
22. Srivastava, A.; Htoon, H.; Klimov, V. I.; Kono, J. Direct Observation of Dark Excitons in Individual Carbon Nanotubes: Inhomogeneity in the Exchange Splitting. *Phys. Rev. Lett.* **2008**, *101* (8), 087402-1–087402-4.
23. Cognet, L.; Tsyboulski, D. A.; Rocha, J.-D. R.; Doyle, C. D.; Tour, J. M.; Weisman, R. B. Stepwise Quenching of Exciton Fluorescence in Carbon Nanotubes by Single-Molecule Reactions. *Science* **2007**, *316*, 1465–1468.
24. Crochet, J. J.; Duque, J. G.; Werner, J. H.; Lounis, B.; Cognet, L.; Doorn, S. K. Disorder Limited Exciton Transport in

Colloidal Single-Wall Carbon Nanotubes. *Nano Lett.* **2012**, *12* (10), 5091–5096.
25. Ma, Y.-Z.; Graham, M. W.; Fleming, G. R.; Green, A. A.; Hersam, M. C. Ultrafast Exciton Dephasing in Semiconducting Single-Walled Carbon Nanotubes. *Phys. Rev. Lett.* **2008**, *101*, 217402.
26. Malic, E.; Weber, C.; Richter, M.; Atalla, V.; Klamroth, T.; Saalfrank, P.; Reich, S.; Knorr, A. Microscopic Model of the Optical Absorption of Carbon Nanotubes Functionalized with Molecular Spiropyran Photoswitches. *Phys. Rev. Lett.* **2011**, *106*, 097401.
27. Wang, F.; Dukovic, G.; Brus, L. E.; Heinz, T. F. Time-Resolved Fluorescence of Carbon Nanotubes and Its Implication for Radiative Lifetimes. *Phys. Rev. Lett.* **2004**, *92*, 177401.
28. Wang, Q. H.; Strano, M. S. Carbon Nanotubes: A Bright Future for Defects. *Nat. Chem.* **2013**, *5*, 812–813.
29. Ghosh, S.; Bachilo, S. M.; Simonette, R. A.; Beckingham, K. M.; Weisman, R. B. Oxygen Doping Modifies near-Infrared Band Gaps in Fluorescent Single-Walled Carbon Nanotubes. *Science* **2010**, *330*, 1656–1659.
30. Miyauchi, Y.; Iwamura, M.; Mouri, S.; Kawazoe, T.; Ohtsu, M.; Matsuda, K. Brightening of Excitons in Carbon Nanotubes on Dimensionality Modification. *Nat. Photonics* **2013**, *7*, 715–719.
31. Piao, Y. M.; Meany, B.; Powell, L. R.; Valley, N.; Kwon, H.; Schatz, G. C.; Wang, Y. H. Brightening of Carbon Nanotube Photoluminescence through the Incorporation of sp^3 Defects. *Nat. Chem.* **2013**, *5*, 840–845.
32. Finnie, P.; Lefebvre, J. Photoinduced Band Gap Shift and Deep Levels in Luminescent Carbon Nanotubes. *ACS Nano* **2012**, *6*, 1702–1714.
33. Iakoubovskii, K.; Nobutsugu, M.; Kim, Y.; K, M.; Kazaoui, S.; Nalini, B. Midgap Luminescence Centers in Single-Wall Carbon Nanotubes Created by Ultraviolet Illumination. *Appl. Phys. Lett.* **2006**, *89*, 173108.
34. Santos, S. M.; Yuma, B.; Berciaud, S.; Shaver, J.; Gallart, M.; Gilliot, P.; Cognet, L.; Lounis, B. All-Optical Trion Generation in Single-Walled Carbon Nanotubes. *Phys. Rev. Lett.* **2011**, *107*, 187401.
35. Harutyunyan, H.; Gokus, T.; Green, A. A.; Hersam, M. C.; Allegrini, M.; Hartschuh, A. Defect-Induced Photoluminescence from Dark Excitonic States in Individual Single-Walled Carbon Nanotubes. *Nano Lett.* **2009**, *9*, 2010–2014.
36. Nagatsu, K.; Chiashi, S.; Konabe, S.; Homma, Y. Brightening of Triplet Dark Excitons by Atomic Hydrogen Adsorption in Single-Walled Carbon Nanotubes Observed by Photoluminescence Spectroscopy. *Phys. Rev. Lett.* **2010**, *105*, 157403.
37. Akizuki, N.; Iwamura, M.; Mouri, S.; Miyauchi, Y.; Kawasaki, T.; Watanabe, H.; Suemoto, T.; Watanabe, K.; Asano, K.; Matsuda, K. Nonlinear Photoluminescence Properties of Trions in Hole-Doped Single-Walled Carbon Nanotubes. *Phys. Rev. B* **2014**, *89*, 195432.
38. Matsunaga, R.; Matsuda, R.; Kanemitsu, Y. Observation of Charged Excitons in Hole-Doped Carbon Nanotubes Using Photoluminescence and Absorption Spectroscopy. *Phys. Rev. Lett.* **2011**, *106*, 037404.
39. Park, J. S.; Hirana, Y.; Mouri, S.; Miyauchi, Y.; Nakashima, N.; Matsuda, K. Observation of Negative and Positive Trions in the Electrochemically Carrier-Doped Single-Walled Carbon Nanotubes. *J. Am. Chem. Soc.* **2012**, *134*, 14461–14466.
40. Kilina, S.; Ramirez, J.; Tretiak, S. Chemical Functionalization and Brightening of Dark Excitons in Semiconducting Carbon Nanotubes. *Nano Lett.* **2012**, *12*, 2306.
41. Ramirez, J.; Mayo, M. L.; Tretiak, S.; Kilina, S. Electronic Structure Calculations and Optical Spectra of Semiconducting Carbon Nanotube Functionalized by Diazonium Systems. *Chem. Phys.* **2013**, *413*, 89.
42. Mu, J.; Ma, Y.; Yin, H.; Liu, C.; Rohlfing, M. Photoluminescence of Single-Walled Carbon Nanotubes: The Role of Stokes Shift and Impurity Levels. *Phys. Rev. Lett.* **2013**, *111*, 137401.
43. Htoon, H.; O'Connell, M. J.; Cox, P. J.; Doorn, S. K.; Klimov, V. I. Low Temperature Emission Spectra of Individual Single-Walled Carbon Nanotubes: Multiplicity of Subspecies within Single-Species Nanotube Ensembles. *Phys. Rev. Lett.* **2004**, *93*, 027401.
44. Tretiak, S. Triplet Absorption in Carbon Nanotubes: A Td-Dft Study. *Nano Lett.* **2007**, *7*, 2201.
45. Galland, C.; Hoegele, A.; Tuereci, H. E.; Imamoglu, A. Non-Markovian Decoherence of Localized Nanotube Excitons by Acoustic Phonons. *Phys. Rev. Lett.* **2008**, *101*, 067402.
46. Vialla, F.; Chassagneux, Y.; Ferreira, R.; Roquelet, C.; Diederichs, C.; Cassabois, G.; Roussignol, P.; Lauret, J. S.; Voisin, C. Unifying the Low-Temperature Photoluminescence Spectra of Carbon Nanotubes: The Role of Acoustic Phonon Confinement. *Phys. Rev. Lett.* **2014**, *113* (5), 057402.
47. Murakami, Y.; Kono, J. Nonlinear Photoluminescence Excitation Spectroscopy of Carbon Nanotubes: Exploring the Upper Density Limit of One-Dimensional Excitons. *Phys. Rev. Lett.* **2009**, *102*, 037401.
48. Xiao, Y.-F.; Nhan, T. Q.; Wilson, M. W. B.; Fraser, J. M. Saturation of the Photoluminescence at Few-Exciton Levels in a Single-Walled Carbon Nanotube under Ultrafast Excitation. *Phys. Rev. Lett.* **2010**, *104*, 017401.
49. Arnold, M. S.; Green, A. A.; Hulvat, J. F.; Stupp, S. I.; Hersam, M. C. Sorting Carbon Nanotubes by Electronic Structure Using Density Differentiation. *Nat. Nanotechnol.* **2006**, *1* (1), 60–65.
50. Ghosh, S.; Bachilo, S. M.; Weisman, R. B. Advanced Sorting of Single-Walled Carbon Nanotubes by Nonlinear Density-Gradient Ultracentrifugation. *Nat. Nanotechnol.* **2010**, *5* (6), 443–450.
51. Kilina, S.; Tretiak, S. Excitonic and Vibrational Properties of Single-Walled Semiconducting Carbon Nanotubes. *Adv. Funct. Mater.* **2007**, *17* (17), 3405–3420.
52. Dewar, M. J. S.; Zoebisch, E. G.; Healy, E. F.; Stewart, J. J. P. Am1: A New General Purpose Quantum Mechanical Molecular Model. *J. Am. Chem. Soc.* **1985**, *107*, 3902.
53. Frisch, M. J.; Trucks, G. W.; Schlegel, H. B.; Scuseria, G. E.; Robb, M. A.; Cheeseman, J. R.; Scalmani, G.; Barone, V.; Mennucci, B.; Petersson, G. A. *et al. Gaussian 09*, Rev. A01, Gaussian, Inc.: Wallingford, CT, 2009.
54. Dukovic, G.; Wang, F.; Song, D.; Sfeir, M. Y.; Heinz, T. F.; Brus, L. E. Structural Dependence of Excitonic Optical Transitions and Band-Gap Energies in Carbon Nanotubes. *Nano Lett.* **2005**, *5* (11), 2314–2318.